

Original Research

Multi-Source Remote Sensing Feature Fusion for Extracting Impervious Urban Surfaces

Jing Ding^o, Xiaodong Ge, Xingda Chen, Wanli Wang,
Guolong Li, Zhen Zhang*

School of Geomatics, Anhui University of Science and Technology, Huainan 232001, China

Received: 5 November 2024

Accepted: 17 March 2025

Abstract

Impervious urban surfaces critically impact ecological environments, necessitating precise and efficient mapping for sustainable urban planning. While hyperspectral remote sensing is widely used for feature extraction, single-source data often face challenges like homospectral heterogeneity and heterospectral homogeneity in complex urban areas. This study addresses these limitations by integrating Zhuhai-1 hyperspectral imagery with Sentinel-1 radar data, proposing an innovative method to enhance impervious surface mapping accuracy through multi-source remote sensing synergy. Further, we compared four tree-based ensemble-learning algorithms for use with multi-source remote sensing data. The results of the pilot study using this approach can be summarized as follows: (1) The four tree-based ensemble learning methods using multi-source remote sensing features perform better than single-source spectral data extraction. Specifically, the Kappa coefficient for the lightweight gradient boosting tree algorithm (LightGBM) in the impervious surface mapping of built-up areas and urban fringes increased by 0.014 and 0.017, respectively. (2) The LightGBM algorithm using multi-source remote sensing features exhibited the best mapping accuracy for extracting impervious surfaces compared to other algorithms, with an accuracy of 93.2% in built-up areas and 92.1% at urban edges. Further, it is also shown to be the most efficient model, with 19.7- and 20.3-second running times in built-up areas and urban edges, respectively. The findings in this study provide a new approach for high-efficiency and high-precision impervious urban surface mapping.

Keywords: impervious surface, LightGBM, machine learning, multi-source, remote sensing

Introduction

Impervious surfaces include roads, driveways, sidewalks, parking lots, and roofs covered by impervious building materials, such as tiles, asphalt, cement concrete, and other materials. Such surfaces

negatively affect the urban ecological environment by replacing the vegetation-based natural landscape, hindering surface water infiltration, and aggravating the surface runoff process [1]. Expanding impervious urban surfaces has significantly impacted urban and near-urban meteorological and hydrological dynamics [2-4]. The heat-absorbing characteristics of artificial building materials and increases in particulate matter in the air alter monsoon patterns. These effects result in surges in rain in the summer, causing urban

*e-mail: zhangzhen@aust.edu.cn

^oORCID iD: 0000-0002-4022-5808

flooding [5]. Additionally, an increase in urban surface runoff due to the expansion of cities carries pollutants (heavy metals, major nutrients, road garbage, and rubber residue) into water bodies, affecting water quality [6]. Rapid urbanization has led to increasingly severe environmental problems. Therefore, the timely and accurate mapping of impervious urban surfaces should be carried out to protect the urban ecological environment.

Numerous studies have been conducted on impervious urban surface classification using two major classification strategies [7, 8]. The first only uses the spectral features from a single satellite sensor, and the second uses multi-source remote sensing features. The rationale of the first strategy is that different land cover types have distinct spectral characteristics, and these spectral features, in turn, could be used for classification. These approaches provide remote sensing images with different spatial resolutions for estimating impervious surfaces [9-12]. However, bare soil, water, and impervious surfaces with low spectral reflectance values usually have similar spectral information, making classification challenging. Furthermore, cloud contamination of optical data poses a significant challenge for accurate land-cover classification. The second strategy utilizes both spectral and SAR data [13, 14], improving classification accuracy. SAR is sensitive to the dielectric and geometric properties of urban land surfaces, including the structure and surface roughness [15]. SAR is also effective at all times and under all weather conditions. Generally, the backscattering intensity of natural features, such as water-permeable and water surfaces, is low; in contrast, urban land with artificial features has high backscattering intensity. Additionally, significant past research has proven that using images derived from InSAR pairs (e.g., coherence) improves the ability to distinguish natural features from man-made ones [16]. This mainly depends on artificial ground features having very high phase stability characteristics and maintaining high coherence over long intervals (35 days or more). In contrast, water bodies, vegetation, and bare land vary within a span of a few days; this indicates that textural features are also helpful when classifying impervious surfaces [17]. Therefore, backscattering intensity, textural features, and data coherence intensity provide complementary information for land-cover classification.

Suitable spatial and spectral resolution satellite data inputs to classifiers are required for accurate classification [18]. The greatly increased dimensionality of a hyperspectral sensor could remove the sensor-related limit on the number of end members available [19]. Furthermore, high spatial resolution image data can achieve high-efficiency and high-precision impervious urban surface mapping [20]. Therefore, the fusion of Zhuhai-1 hyperspectral data (with a spatial resolution of 10 m and 32 bands) and Sentinel-1 radar data could effectively overcome the limitations concerning spectral information in classifying complex urban areas [21].

Previous studies based on the V-I-S model used remote sensing images for impervious surface mapping [22]. The V-I-S method simplifies land surface classification and enhances processing efficiency and extraction accuracy. It is widely applied in remote sensing image analysis, particularly for extracting impervious urban surfaces. However, complex ground features hinder the application of the V-I-S model in extracting impervious urban surfaces from high-resolution remote sensing images. Therefore, researchers have proposed extraction methods that effectively integrate machine learning techniques to handle high-resolution remote sensing images [23, 24]. Various ML-based approaches have been conducted to extract impervious surfaces, such as the support vector machine (SVM) and convolutional neural network (CNN) [25, 26]. The aforementioned methods have achieved good results and have been widely applied.

Recent studies have reported that tree-based ensemble-learning algorithms (e.g., random forest [RF], gradient boosting decision tree [GBDT], extreme gradient boosting [XGBoost], and the lightweight gradient boosting tree algorithm [LightGBM]) are more effective than other ML-based approaches [27-29]. Tree-based ensemble models are relatively simple but powerful algorithms for classification and regression problems. They have been widely applied in the fields of agriculture, landslide susceptibility mapping, forecasting, and analysis of daily average PM_{2.5} concentrations [30-32]. However, there is little relevant research in the field of the extraction of impervious urban surfaces.

Therefore, this study applies tree-based ensemble-learning algorithms to extract and estimate impervious urban surfaces. Zhuhai-1 hyperspectral images combined their spectral data, and Sentinel-1 radar data was used as the feature data. From these, 11 characteristic bands were identified and selected, including eight spectral features, two radar data features, and one spatial texture feature. The eight spectral features correspond to the first eight hyperspectral bands with a contribution rate greater than 75% through the minimum noise fraction rotation (MNF) transform. Based on the data of GF-1 (Gaofen-1) images, the artificial vectorization label of GF-1 is used to study RF, GBDT, XGBoost, and LightGBM algorithms for mapping impervious urban surfaces. The findings of this study provide a feasible and efficient method for building a sponge city with natural accumulation, penetration, and purification abilities.

Materials and Methods

Study Area

Suzhou City is in the southern plain of Jiangsu Province, China. It is characterized by several water systems and has a mild climate, distinct seasons,

and abundant rainfall. A water transportation system is present in this region, which is often referred to as a “water village”. Suzhou has experienced rapid urbanization and has a complex construction environment. This urban expansion has contributed to increased impervious surface areas, leading to various environmental and socio-economic concerns.

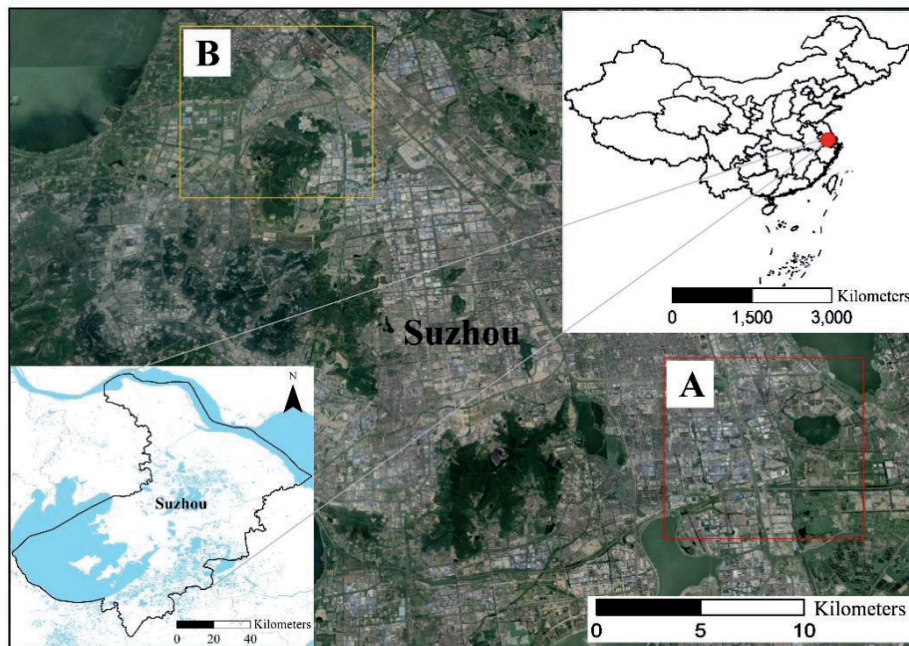
Therefore, there is a need to map high-efficiency and high-precision impervious urban surfaces in this region. However, separating water from impervious surfaces with low spectral reflectance is challenging, and bare soil and impervious surfaces are often easily conflated. Furthermore, extracting small water bodies is a difficult task. Thus, two regions in the built-up area of Suzhou and the city fringes (with more bare soil and small water bodies) were selected as the experimental areas (Fig. 1).

Fig. 1A) shows a portion of the built-up area. The study site comprises various ground objects, such

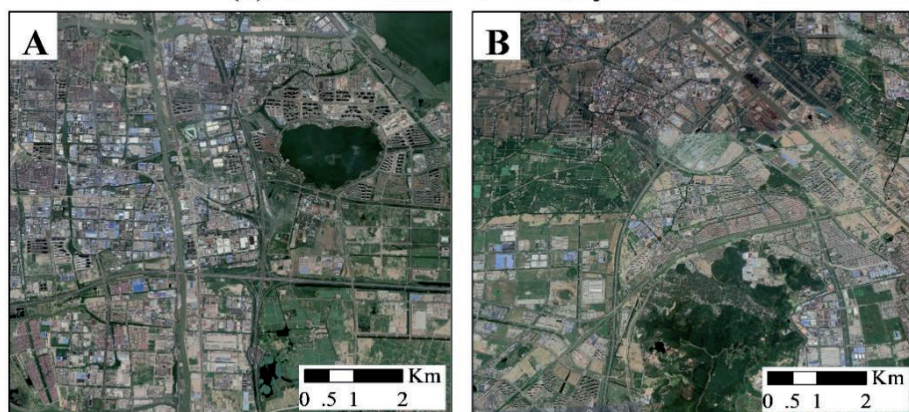
as water bodies, polluted water bodies, buildings, roads, vegetation, and bare soil. The image size in this figure is 742×824 pixels. Fig. 1B) represents the urban fringe areas. The region is covered in bare soil, small water bodies, and densely packed buildings. The image size here is 775×834 pixels.

Hyperspectral Data Reprocessing

Zhuhai Orbit Corporation provided the hyperspectral remote sensing images of Suzhou City used in this study (<https://www.myorbita.net>) on October 1, 2018. The second batch of Zhuhai-1 microsattellites was successfully launched on April 26, 2018. This batch included four Orbita hyperspectral satellites (i.e., OHS-A, OHS-B, OHS-C, and OHS-D) and one video satellite (i.e., OVS-2A) with excellent hyperspectral data acquisition abilities. The hyperspectral satellite



(a) Overview of the study area



(b) Two experimental areas

Fig. 1. Overview of the study area with a) a built-up area and b) an urban fringe.

camera can obtain images with a 10-m resolution, 150-km width, and 32 spectrum segments. The single-start continuous sweeping work time was no less than 2 min, and the one-track working time was no more than 8 min, with a global coverage ability within 5 days [33]. Rich spectral information is important for the extraction and classification of the features of ground objects. The spatial scale of the image was suitable for city-wide research.

Radiation calibration, atmospheric correction (ENVI Fast Line-of-sight Atmospheric Analysis of Hypercubes (FLAASH) module), and orthographic correction were carried out on hyperspectral data. Additionally, Gaussian low-pass filtering was used to filter orthographic hyperspectral images and eliminate the effect of geometric distortion and noise in satellite imaging. Hyperspectral data were geographically registered with GF-1 data, leading to a one-to-one correspondence of the spectral features to the classification labels. Minimum noise fraction rotation (MNF) transformation was performed on the hyperspectral data to eliminate redundancy and reduce the number of calculations during classification. The amount of hyperspectral data used in this experiment was large. Therefore, we concentrated on the remote sensing feature information within a few bands. The first eight bands, with a contribution rate greater than 75%, were used as the remote sensing spectral features in this study. The spatial co-occurrence

measures of hyperspectral remote sensing images in the study area were calculated to obtain the spatial texture information. This was done to achieve spatial spectrum integration and fully extract spectral information from the optical remote sensing images. Fig. 2 shows the hyperspectral curves of several typical features of Zhuhai-1 after data reprocessing.

SAR Data Reprocessing

The Sentinel-1 radar data was provided by the European Space Agency (<https://search.asf.ala-ska.edu>). The primary imaging time was October 1, 2018, while the secondary imaging time was November 6, 2018.

The radar backscatter intensity and radar interference information supplement the thematic information of the urban features. Backscatter intensity data were obtained after radiometric calibration on October 1, 2018. Additionally, we obtained interference coherence from the long-time-baseline (35 days) interferometric radar signal using the differential interferometry synthetic aperture radar (D-InSAR) process [34]. The fusion of Sentinel-1 radar feature data and Zhuhai-1 hyperspectral feature data was used as mapping data, and the tree-based ensemble-learning algorithm was used to extract impervious urban surfaces. The process is shown in Fig. 3.

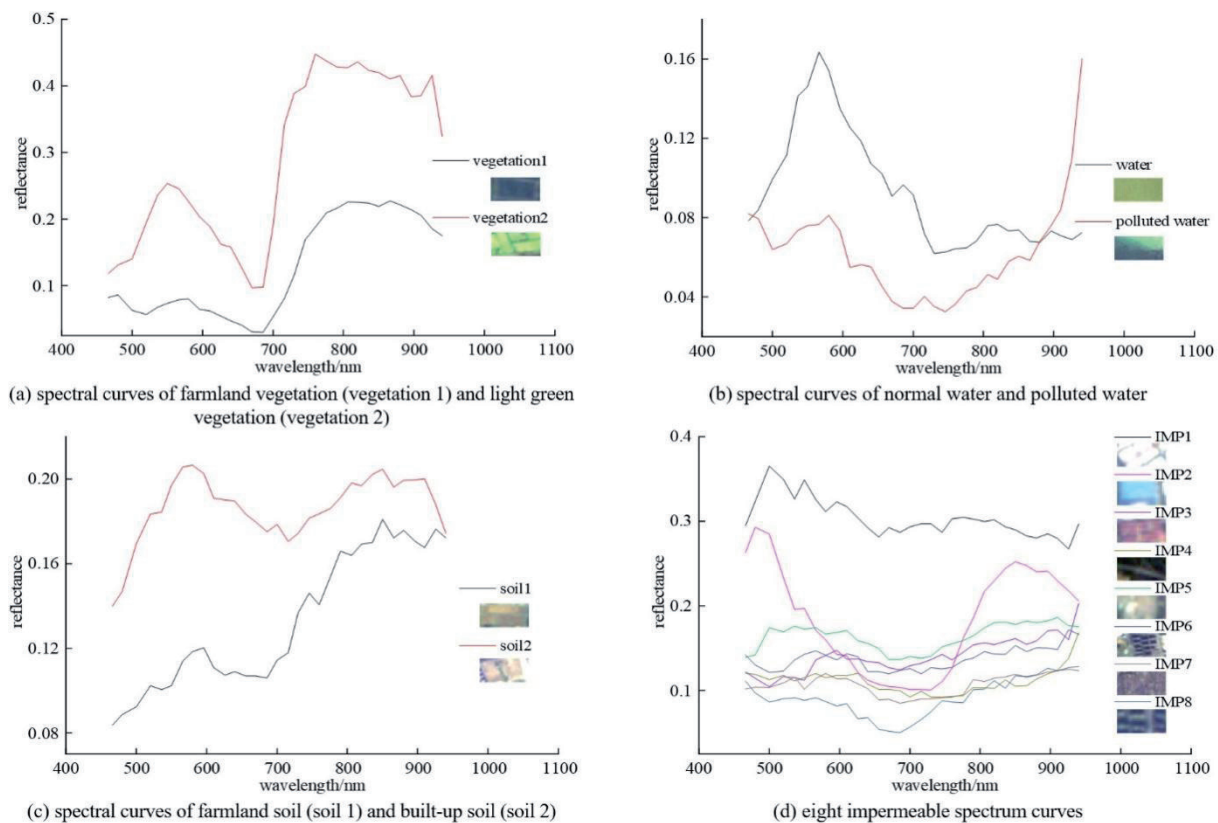


Fig. 2. Hyperspectral curves of typical features of Zhuhai-1.

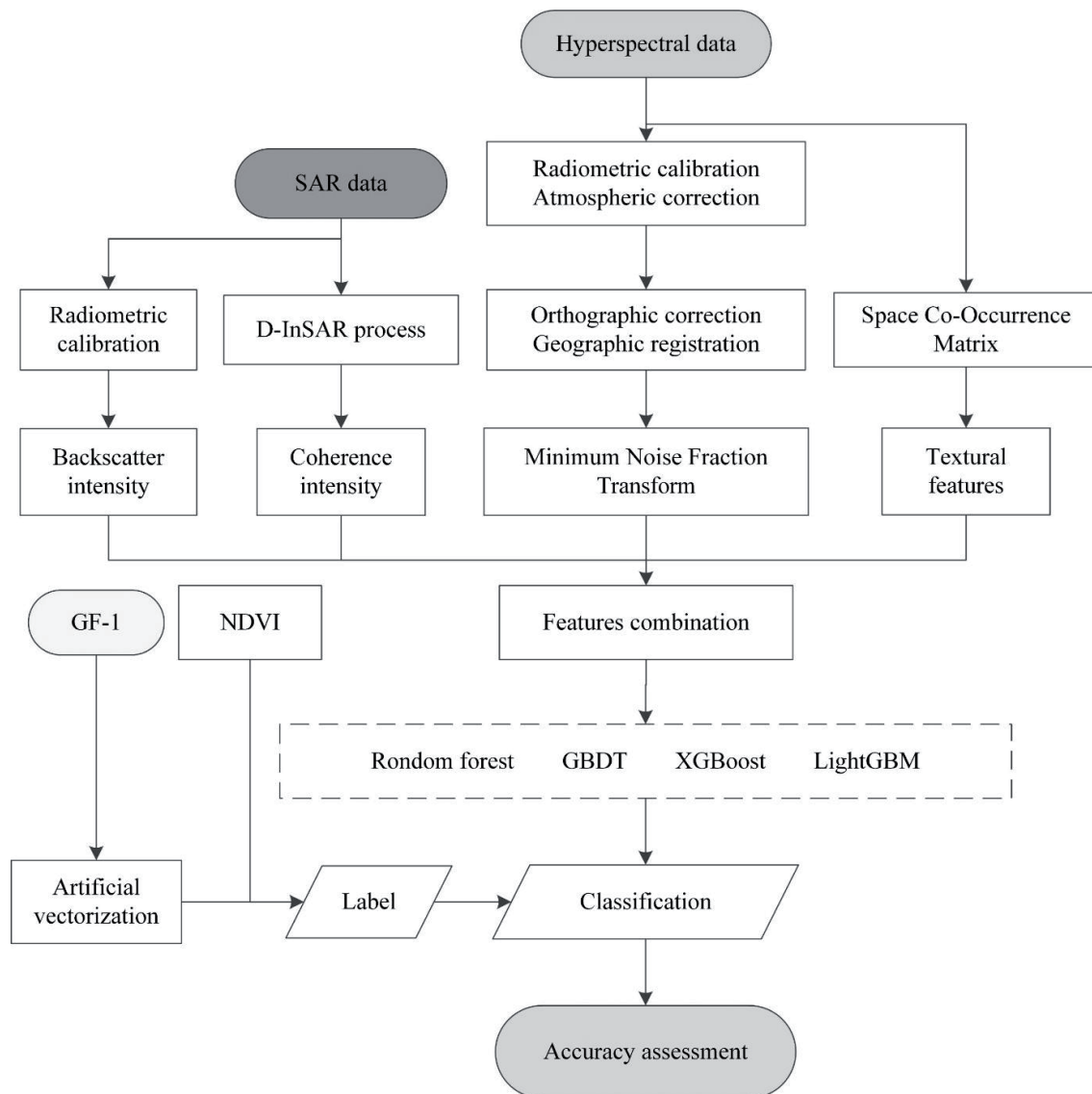


Fig. 3. Flowchart of the process of this study.

Artificial Vectorization Label

GaoFen1 (GF1), China's first high-resolution Earth observation satellite, was launched in April 2013. This satellite has one panchromatic sensor and four wide field-of-view (WFV) sensors [35]. A single image collected by one sensor has a swath of nearly 200 km. Therefore, when all four sensors collect images simultaneously, an area with a total width of 800 km can be covered, allowing the satellite to achieve global coverage in four days [36].

We acquired GF-1 data from the study area during the survey period. The data were fused with the panchromatic and multispectral bands, followed by ortho-correction. The processed GF-1 data (with a spatial resolution of 2 m) was artificially vectorized. The land cover in the study area was then divided into three types: impervious surfaces, permeable surfaces, and water surfaces (Fig. 4). In this study, the intensity data, the coherence intensity map, and vectorized labels

were resampled to a spatial resolution of 10 m to ensure that data fusion and classification evaluation took place under the same spatial resolution.

Principles of the Tree-based Ensemble-Learning Algorithm Using Multi-source Remote Sensing Features

Tree-based ensemble learning is an algorithm that creates a strong assessment model by integrating multiple weak assessment models [37]. It is highly accurate, effective for processing high-dimensional big data, and stable in terms of model training. Each weak learner (decision tree) calculates the gain of each feature during node splitting and selects the feature with the best gain value for splitting.

In this study, the tree-based ensemble-learning algorithm classifies fused multi-source remote sensing feature data pixel-by-pixel to obtain a highly precise and efficient thematic map of impervious urban

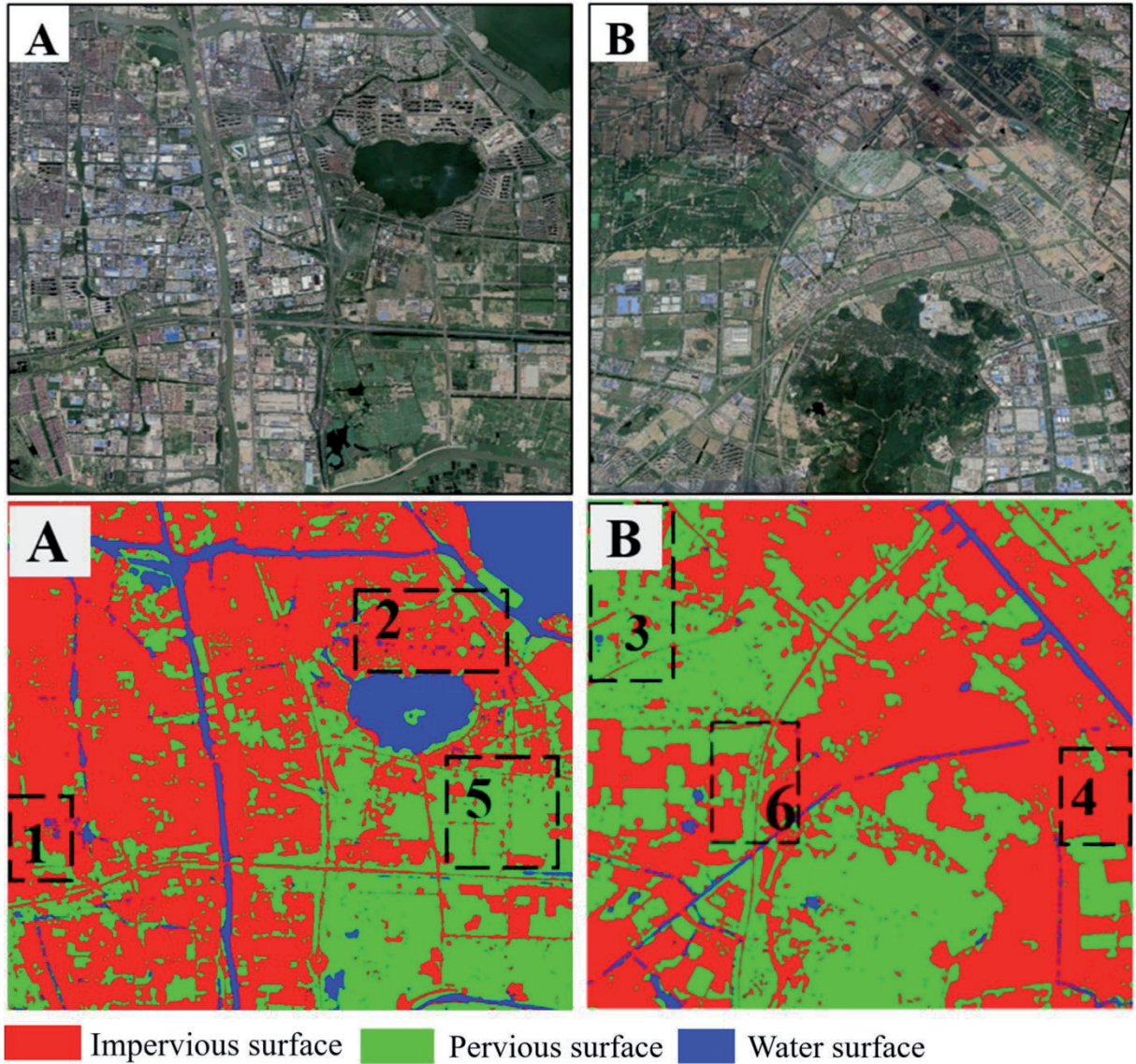


Fig. 4. Results of artificial vectorization labeling for (a) a built-up area and (b) an urban fringe.

surfaces. The first eight bands, the 9th band, the 10th band, and the 11th band denote the spectral features, interference coherence characteristic magnification with a value scaled up by 100-fold, backscatter intensity, and the spatial texture features, respectively (Fig. 5). The results show that impervious surface objects have high coherence (with coherence coefficients greater than 0.5). Bare soils in built-up areas and polluted waters have high coherence and unique spectral characteristics, whereas general natural ground objects have low coherence. Thus, the fusion of SAR data features and Zhuhai-1 hyperspectral data enhanced the selection of the segmentation node of the tree-based ensemble-learning algorithm.

Principle of the XGBoost Algorithm

GBDT is a tree-based ensemble algorithm that builds an integrated prediction model through the gradient

boosting process. The specific principle behind this algorithm has been expounded in previous research [38]. In comparison to the classic GBDT, XGBoost has significantly better performance. Firstly, GBDT expands the objective Taylor function to the first order, while XGBoost expands the objective Taylor function to the second order. More information about the objective function is retained, which improves the performance. Secondly, XGBoost introduces the regularization term in the objective function to prevent overfitting. The principle of the algorithm is as follows:

Loss function

$$L = \sum_i^n l(y_i, \hat{y}_i) \quad (1)$$

where n , \hat{y} , and y are the number of input training samples, predicted value, and label, respectively.

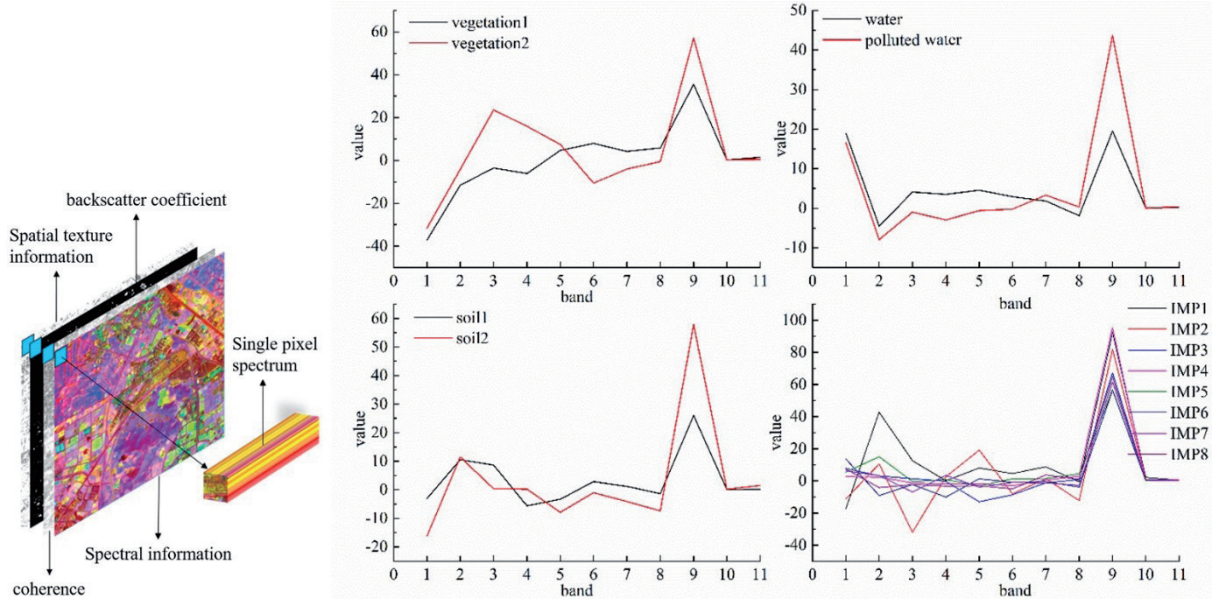


Fig. 5. Typical features of multi-source remote sensing (Fig. 4 ground objects correspond to Fig. 2).

Objective function

$$Obj = L + \Omega(\theta) \quad (2)$$

where $\Omega(\theta)$ is the regularization term to prevent model overfitting. The objective function uses T-base classification tree models: $\{f_1, f_2, \dots, f_T\}$. We assume that the predicted value of the i-th input sample is $\hat{y}_i = \sum_{t=1}^T f_t(x_i)$, where x_i is the input sample and \hat{y}_i is the corresponding predicted value. Therefore

$$Obj = \sum_i^n l(y_i, \hat{y}_i) + \sum_{t=1}^T \theta(f_t) \quad (3)$$

Ensemble-learning algorithms use errors as optimization criteria. Taylor's second-order approximation expands the loss function to establish a link between the node-splitting guidelines of the binary tree model and the objective function:

$$\sum_{i=1}^n l(y_i, \hat{y}_i^{T-1} + f_T(x_i)) = \sum_{i=1}^n [l(y_i, \hat{y}_i^{T-1}) + l'(y_i, \hat{y}_i^{T-1})f_T(x_i) + \frac{1}{2}l''(y_i, \hat{y}_i^{T-1})f_T^2(x_i)] \quad (4)$$

The XGBoost algorithm is shown in Fig. 6.

Principle of LightGBM

The LightGBM algorithm is an optimization algorithm for the XGBoost algorithm. Unlike the XGBoost algorithm, the LightGBM algorithm uses a histogram optimization method to discretize the feature data. The histogram optimization method

mitigates this limitation in that the split node in the base classification model needs to sort all of the feature data. Meanwhile, this algorithm supports a parallel strategy.

The LightGBM algorithm structure is shown in Fig. 7.

Sample Data

The urban cover in the study area is divided into impermeable surfaces, permeable surfaces, and water surfaces (with a ratio close to 1:1:1). We used manual interpretation to select the training samples and classification evaluation samples based on field survey data and high-resolution GF-1 images obtained during the survey period. Data were scrambled and dichotomized into "train" (66.7% of the data) and "test" (33.3% of the data) sets. Details of the selected samples are given in Table 1.

The range of common hyperparameter values for the ensemble algorithms used is shown in Table 2.

Results

Experimental Results and Accuracy Assessment

We carried out eight comparative tests to demonstrate the superiority of the LightGBM model using multi-source remote sensing features. The four algorithms performed surface extraction experiments on the single-source spectral feature data and multi-feature remote sensing data. Pixel-level classification caused a salt-and-pepper effect; therefore, post-classification processing technology eliminated false pixels generated during classification.

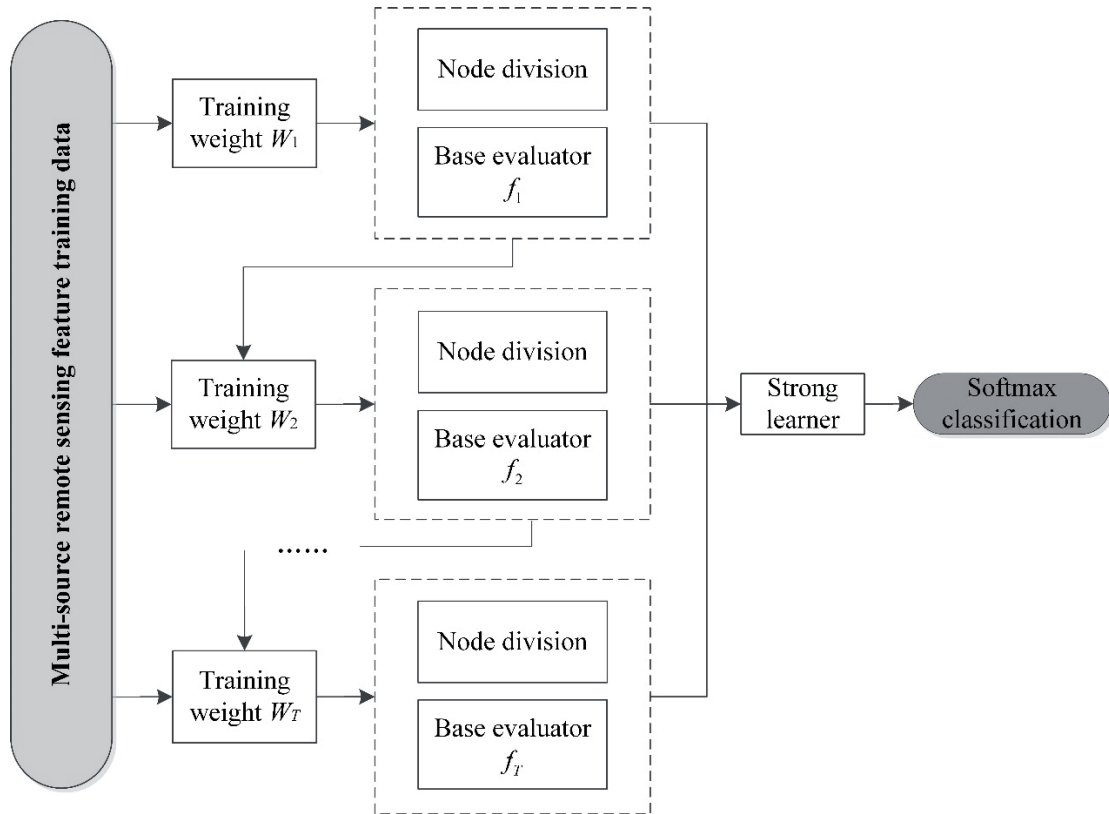


Fig. 6. XGBoost algorithm flowchart.

As indicated by tags 1-4 in Fig. 8a), the random forest algorithm – which fused multi-source remote sensing feature data – was used to map the impervious surface. This algorithm mistakenly classified impervious urban surfaces with low reflectances as water surfaces. The GBDT, XGBoost, and LightGBM algorithms, based

on the gradient boosting tree algorithm, give better descriptions of the edge information of the urban cover than the random forest algorithm (tag 5 in Fig. 8). Additionally, these algorithms retain the structural information of impermeable surfaces better and greatly reduce the conflation of impermeable surfaces and water

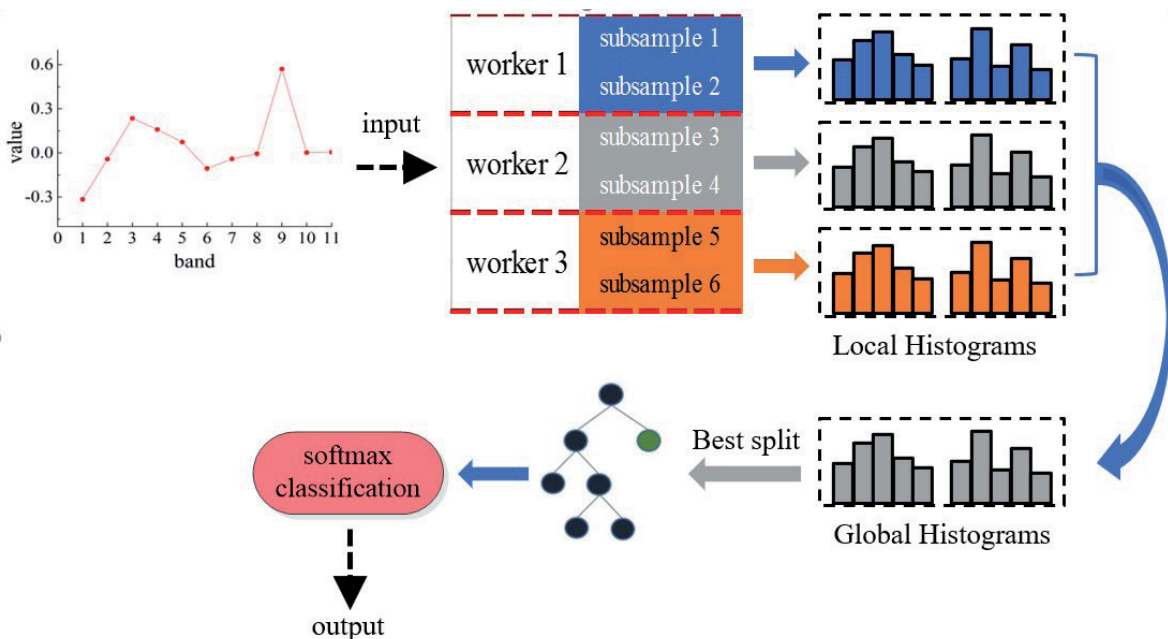


Fig. 7. LightGBM algorithm flowchart.

Table 1. Sample details (number of pixels).

Category	Built-up area		Urban fringes	
	Train	Test	Train	Test
Impervious surface	35724	17862	35724	17862
Pervious surface	34267	17136	34267	17136
Water surface	32916	16459	32916	16459

Table 2. Hyperparameter values of ensemble-learning algorithms.

Category	Hyperparameter ranges
Learning rate	0.01, 0.05, 0.1, and 0.5
Min samples leaf	1 to 21 (increment of 1)
Max depth	1 to 15 (increment of 1)
Subsample	0.2 to 1 (increment of 0.1)
Number of estimators	10, 100, 200, and 1000

surfaces compared with the random forest algorithm. The XGBoost and LightGBM algorithms performed better in dividing bare soil and buildings, with the lowest misclassification and improved retention of edge information, as shown by the true label with tag 6. The XGBoost and LightGBM algorithms expand the objective Taylor function to the second order. This retains more information about the objective function, which improves the performance. However, overly small water bodies were difficult to extract from remote sensing data based on a 10-meter spatial resolution in urban boundary areas. Further, discriminating between bare soil and impervious surfaces was challenging.

We quantified the mapping precision of extracting the urban cover to quantitatively analyze the extraction effects of the four algorithms. The extraction results of the four ensemble-learning algorithms used in this study were compared with the real labels. Table 3 provides discernible information regarding four pixel-based classifiers. The random forest algorithm had the highest misclassification rates, with 2.12%, 2.04%, and 0.09% errors in terms of impervious surfaces, pervious surfaces, and water surfaces, respectively. The XGBoost and LightGBM algorithms performed better in terms of mapping the impervious urban surfaces with multi-source remote sensing data. Notably, LightGBM was found to be the best classification model, with 1.56%, 1.33%, and 0.22% errors in the impervious surfaces, pervious surfaces, and water surfaces, respectively.

Result Analysis

The overall accuracy (OA) and Kappa coefficient of the four ensemble-learning classification model methods were calculated using a confusion matrix. The coefficient measures the results of the impervious surface extraction. The analysis showed that the four

ensemble-learning algorithms fused multi-source remote sensing features and improved impervious urban surface mapping performance compared to only using spectral features (Table 4). From Table 4, it can be seen that compared to the single-source data, the OA of the LightGBM using multi-source remote sensing features was improved by 3.6% and 4.6% in the built-up areas and urban fringes, respectively. Furthermore, the Kappa coefficient was increased by 0.014 and 0.017 in the built-up areas and urban fringes, respectively. In the single-source spectral data extraction process, these models ignored the homologous heterospectra and homospectral foreign objects in the complex urban environment. However, radar backscatter intensity information and radar interference information supplement the thematic information regarding urban features.

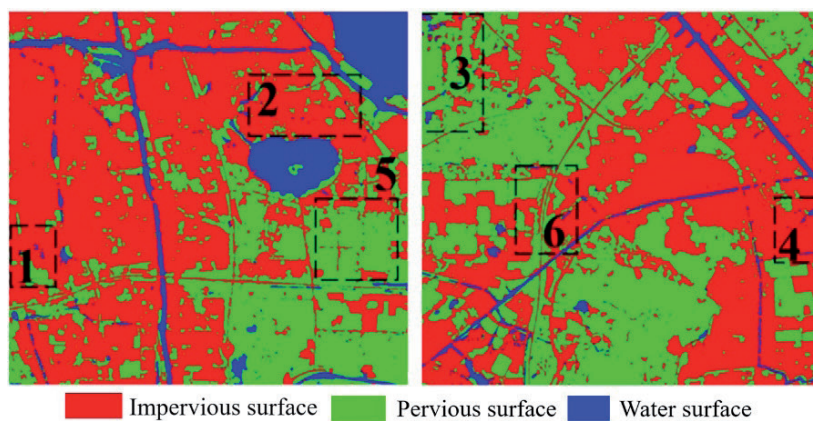
Based on the gradient boosting tree algorithm, the GBDT, XGBoost, and LightGBM algorithms performed better than the random forest algorithm [39-41]. The XGBoost algorithm performed better than the GBDT. Firstly, the loss function of the XGBoost expanded by Taylor's second-order approximation is more precise than Taylor's first-order approximation. Moreover, depending on the leaf node weight and the tree depth, the complexity of the binary tree model in XGBoost differs. LightGBM was more efficient than XGBoost, with a 235.4- and 257.7-second improvement in the built-up areas and urban fringes, respectively. The LightGBM algorithm uses a histogram optimization method to discretize the feature data, unlike the XGBoost algorithm. The histogram optimization method alleviates the limitation whereby the split nodes in the base classification model need to sort all the feature data.

In summary, the LightGBM algorithm using multi-source remote sensing features achieved optimum results with 93.2% and 92.1% OA in the built-up areas and urban fringes and 0.885 and 0.845 Kappa coefficients in the built-up areas and urban fringes, respectively.

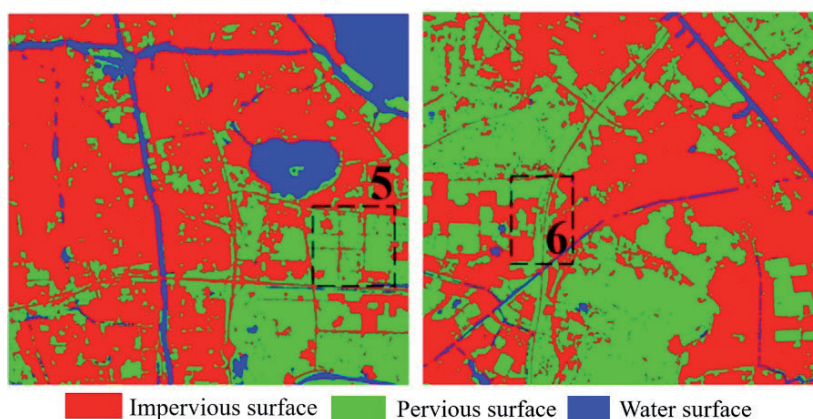
Discussion

Classification of Images

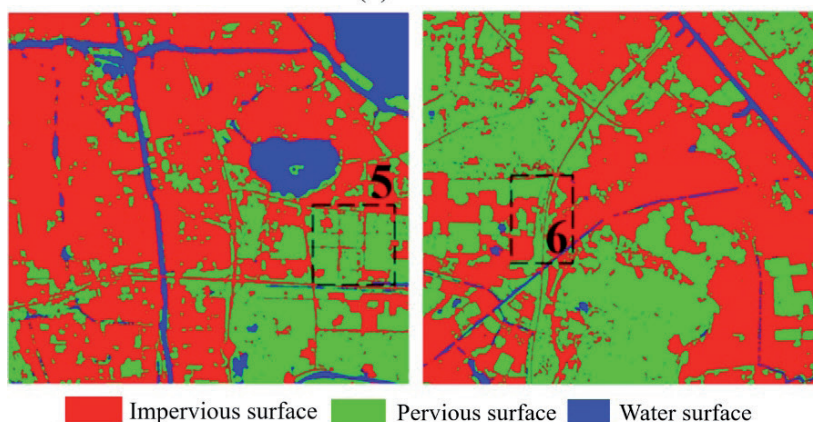
Considering previous studies, remotely sensed data used for impervious classifications could be classified into three types based on spatial resolution: coarse, medium, and high [42]. Because of their high temporal resolution, coarse spatial-resolution data (e.g., MODIS) are only suitable for large-scale remote sensing applications or as an auxiliary source for local and regional data [43]. Medium spatial-resolution data (e.g., SPOT4 and Landsat) can be applied in regional land-cover classification, which comprises a large number of mixed pixels because of the presence of complex ground coverings. High-spatial-resolution data (e.g., WorldView, IKONOS, and QuickBird) could help acquire accurate ground-object classification in complex



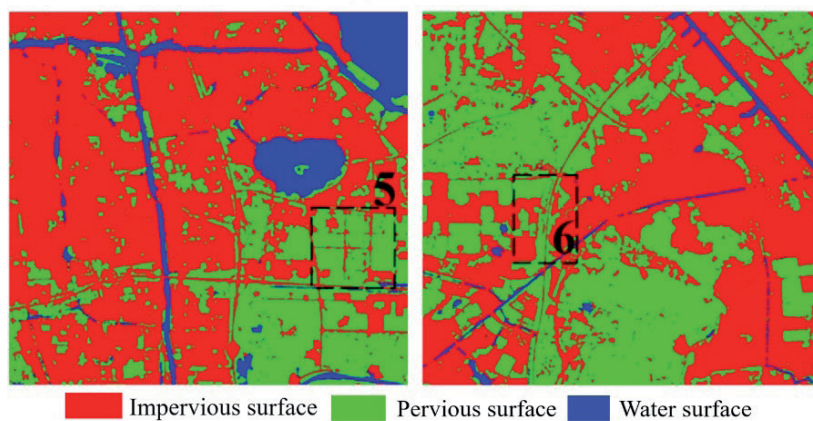
(a) Random forest



(b) GBDT



(c) XGBoost



(d) LightGBM

Fig. 8. Classification results of the four ensemble-learning algorithms.

Table 3. Mapping accuracy of impervious surfaces using four algorithms.

Category	Impervious surface		Pervious surface		Water surface	
	Percentage	Error	Percentage	Error	Percentage	Error
Label	61.99	/	27.17	/	10.84	/
RF	59.87	2.12	29.21	2.04	10.93	0.09
GBDT	63.82	1.83	25.43	1.74	10.65	0.19
XGBoost	63.55	1.56	25.85	1.32	10.60	0.24
LightGBM	63.55	1.56	25.84	1.33	10.62	0.22

Table 4. Accuracy evaluation parameters of the multi-feature fusion ensemble learning method.

Features (a)	Category	Overall accuracy (%)		Kappa		Time (s)	
		Built-up area	Urban fringe	Built-up area	Urban fringe	Built-up area	Urban fringe
Spectral (8 bands)	Random forest	84.6	83.7	0.803	0.794	48.4	51.4
	GBDT	86.7	85.6	0.822	0.812	37.8	42.5
	XGBoost	89.4	87.0	0.871	0.824	209.0	219.0
	LightGBM	89.6	87.5	0.871	0.828	19.6	20.8
Spectral (8 bands) spatial texture (2) SAR (1)	Random forest	90.5	89.7	0.824	0.801	74.5	83.9
	GBDT	91.6	90.9	0.837	0.826	45.6	51.2
	XGBoost	92.9	91.8	0.880	0.839	255.1	278.0
	LightGBM	93.2	92.1	0.885	0.845	19.7	20.3

urban environments. Moreover, previous studies have used remote sensing image series to improve classification accuracy. However, spectral data is easily affected by clouds and weather, resulting in issues with satellite imaging. Instead, a uni-temporal image could rapidly establish a regional impervious map with fewer restrictions and less data computation [42]. Furthermore, the hyperspectral data could remove the limit on the number of end members available. Therefore, we selected uni-temporal Zhuhai-1 hyperspectral data (spatial resolution of 10 m and 32 bands). This strategy utilizes both spectral and SAR data [13, 14], improving the classification accuracy compared to only using the spectral features from a single satellite sensor. Using hyperspectral data in complex urban environments, the latter ignores the homologous heterospectra and homospectral foreign objects.

Classification Methods

In previous studies, image classification methods applied in impervious classifications include sub-pixel-based methods (e.g., the V-I-S model) [22], object-based methods [43], and machine learning algorithms [23-26]. Nevertheless, sub-pixel-based methods are only suitable for an original low-resolution image. Users should know how to select the segmentation scale and which features

must be selected before using an object-oriented method. These two factors substantially determine classification accuracy and computational efficiency [44]. ML-based approaches (e.g., SVM, CNN, tree-based ensemble-learning algorithms) applied to high-resolution images have high classification accuracy. Furthermore, tree-based ensemble-learning algorithms are more effective than other ML-based approaches [27-29]. Notably, LightGBM is the most efficient among tree-based ensemble-learning algorithms because it uses a histogram optimization method to discretize the feature data, improving the algorithm's efficiency. Previous studies have evaluated other machine learning algorithms for impervious surface mapping with approximately 90% accuracy [45]. Although the extraction effect is comparable, the mapping process takes longer to achieve higher accuracies. Therefore, the LightGBM algorithm uses multiple remote sensing features for complete impervious urban surface mapping with high precision and efficiency compared to those reported in previous studies.

Classification Results

Impervious urban surfaces are key factors that shape urban ecological environments [46, 47]. Research into high-precision and high-efficiency impervious urban

surface mapping methods is important for guiding the construction of urban ecological environments [48, 49]. The results of this study show that the fusion of Zhuhai-1 spectral features, spatial texture features, and SAR data features improves the precision and efficiency of the extraction of impervious urban surfaces. The fusion had an overall accuracy of 93.2% in the built-up areas and 92.1% at the urban edges. Our methods rely on spectral features, spatial texture features, and SAR data features obtained from hyperspectral images and radar data. Therefore, they can be used in different urban environments. The findings of this study provide information for the application of ensemble-learning algorithms in automated remote sensing applications [50].

The random forest algorithm using only spectral features provides a satisfactory classification effect for impervious surfaces, with an OA value of 84.6%. This is important when considering using spectral sensors to map impervious surfaces. However, ensemble-learning algorithms based on gradient boosting have better mapping effects. Combining multi-source remote sensing features could achieve a higher segmentation effect when classifying impervious urban surfaces than only using spectral features. Mapping permeable surfaces and water surfaces could yield different results. The mapping error percentages of the GBDT algorithm, XGBoost algorithm, and LightGBM algorithm after adding the SAR feature and texture feature data were relatively close (1.83%, 1.56%, and 1.56%, respectively). Furthermore, adding the SAR and texture feature data improved the OA of the random forest algorithm, GBDT algorithm, XGBoost algorithm, and LightGBM algorithm by 5.9%, 4.9%, 3.5%, and 3.6% in the built-up area, respectively. Moreover, the algorithm using multi-source remote sensing features also performed better than a single source for urban fringes. Thus, SAR data features and spatial texture features improve classification accuracy. However, the addition of the SAR feature and texture feature data does not eliminate the phenomenon of mixed pixels and spectral confusion. ML is a data-driven approach [51]; therefore, this problem can be alleviated by collecting more training samples at the fringes between the low-reflectivity impervious surface, the low-reflectivity water surface, the impervious surface, and vegetation to facilitate discrimination [52, 53].

On the urban fringes, extremely small water bodies are difficult to accurately extract from remote sensing data based on a 10-m spatial resolution [54, 55]. Although the fusion of multi-source remote sensing features improves the discrimination between bare soil and impervious surfaces, the accurate distinction remains challenging [56].

In this study, the LightGBM algorithm using multi-source remote sensing features exhibited high efficiency and mapping accuracy in extracting impervious surfaces [57].

Conclusions

This study reports a new high-precision and high-efficiency impervious urban surface extraction method suitable at a 10-m spatial resolution. Multi-source remote sensing features (i.e., Zhuhai-1 and Sentinel-1 radar data) are used to extract impervious urban surfaces using the LightGBM algorithm. This article focused on Suzhou as the study area, and the following conclusions could be drawn:

(1) The fusion of Zhuhai-1 hyperspectral features with spatial texture features and Sentinel-1 radar data features performs better at extracting impervious urban surfaces than simply using Zhuhai-1 spectral characteristics.

(2) The XGBoost and LightGBM algorithms use the gradient boosting tree principle and combine multi-source remote sensing features to extract impervious urban surfaces. Their performance is better than that of the GBDT and random forest algorithms. The LightGBM algorithm, in particular, exhibited the highest accuracy and efficiency.

This research contributes to developing advanced and efficient methods for urban surface classification, particularly in the context of urban planning and environmental monitoring. By improving the accuracy and efficiency of impervious surface extraction, the proposed method holds significant potential for supporting smart city initiatives, urban heat island studies, and sustainable urban development. Furthermore, it demonstrates the effective integration of multi-source remote sensing data, which can be applied to other urban regions globally, especially in developing countries or regions with limited data availability. The method's adaptability and efficiency make it suitable for a wide range of geographical areas, providing a robust tool for urban studies, environmental management, and policy-making in different countries and regions.

Acknowledgments

This research was funded by the Natural Science Research Project of the Anhui Educational Committee (No.2024AH050367).

Conflict of Interest

The authors declare no conflict of interest.

References

1. YUAN F., BAUER M.E. Comparison of impervious surface area and normalized difference vegetation index as indicators of surface urban heat island effects in Landsat imagery. *Remote Sensing of Environment*. **106** (3), 375, 2007.

2. YU H., ZHAO Y., FU Y. Optimization of impervious surface space layout for prevention of urban rainstorm waterlogging: A case study of Guangzhou, China. *International Journal of Environmental Research and Public Health*. **16** (19), 3613, **2019**.
3. LIU S., GU G. Improving the impervious surface estimation from hyperspectral images using a spectral-spatial feature sparse representation and post-processing approach. *Remote Sensing*. **9** (5), 456, **2017**.
4. XU R., LIU J., XU J. Extraction of high-precision urban impervious surfaces from sentinel-2 multispectral imagery via modified linear spectral mixture analysis. *Sensors*. **18** (9), 2873, **2018**.
5. MCGRANE S.J. Impacts of urbanisation on hydrological and water quality dynamics, and urban water management: a review. *Hydrological Sciences Journal*. **61** (13), 2295, **2016**.
6. TONG S.T., CHEN W. Modeling the relationship between land use and surface water quality. *Journal of Environmental Management*. **66** (4), 377, **2002**.
7. CAO X., GAO X., SHEN Z., LI R. Expansion of urban impervious surfaces in Xining city based on GEE and Landsat time series data. *IEEE Access*. **8**, 147097, **2020**.
8. GUO X., ZHANG C., LUO W., YANG J., YANG M. Urban impervious surface extraction based on multi-features and random forest. *Ieee Access*. **8**, 226609, **2020**.
9. LI L., LU D., KUANG W. Examining urban impervious surface distribution and its dynamic change in Hangzhou metropolis. *Remote Sensing*. **8** (3), 265, **2016**.
10. HENITS L., MUCSI L., LISKA C.M. Monitoring the changes in impervious surface ratio and urban heat island intensity between 1987 and 2011 in Szeged, Hungary. *Environmental Monitoring and Assessment*. **189**, 1, **2017**.
11. PIYOOSH A., SK G. Semi-automatic mapping of anthropogenic impervious surfaces in an urban/suburban area using Landsat 8 satellite data. *GIScience & Remote Sensing*. **54** (4), 1, **2017**.
12. ZHANG L., WENG Q., SHAO Z. An evaluation of monthly impervious surface dynamics by fusing Landsat and MODIS time series in the Pearl River Delta, China, from 2000 to 2015. *Remote Sensing of Environment*. **201**, 99, **2017**.
13. SHAO Z., FU H., FU P., YIN L. Mapping urban impervious surface by fusing optical and SAR data at the decision level. *Remote Sensing*. **8** (11), 945, **2016**.
14. XU R., ZHANG H., LIN H. Urban impervious surfaces estimation from optical and SAR imagery: A comprehensive comparison. *IEEE Journal of Selected Topics in Applied Earth Observations and Remote Sensing*. **10** (9), 4010, **2017**.
15. ZHANG H., LIN H., WANG Y. A new scheme for urban impervious surface classification from SAR images. *ISPRS Journal of Photogrammetry and Remote Sensing*. **139**, 103, **2018**.
16. YANG L., JIANG L., LIN H., LIAO M. Quantifying sub-pixel urban impervious surface through fusion of optical and InSAR imagery. *GIScience & Remote Sensing*. **46** (2), 161, **2009**.
17. VOISIN A., KRYLOV V.A., MOSER G., SERPICO S.B., ZERUBIA J. Classification of very high resolution SAR images of urban areas using copulas and texture in a hierarchical Markov random field model. *IEEE Geoscience and Remote Sensing Letters*. **10** (1), 96, **2012**.
18. CAI Y., GUAN K., PENG J., WANG S., SEIFERT C., WARDLOW B., LI Z. A high-performance and in-season classification system of field-level crop types using time-series Landsat data and a machine learning approach. *Remote Sensing of Environment*. **210**, 35, **2018**.
19. LÓPEZ A., OGAYAR C.J., FEITO F.R., SOUSA J.J. Classification of Grapevine Varieties Using UAV Hyperspectral Imaging. *Remote Sensing*. **16** (12), 2103, **2024**.
20. WENG Q. Remote sensing of impervious surfaces in the urban areas: Requirements, methods, and trends. *Remote Sensing of Environment*. **117**, 34, **2012**.
21. LI C., XIONG X., WANG L., LI Y., WANG J., ZHANG X. Exploring the Potential of the Hyperspectral Remote Sensing Data China Orbita Zhuhai-1 in Land Cover Classification. *Photogrammetric Engineering & Remote Sensing*. **90** (10), 611, **2024**.
22. RIDD M.K. Exploring a VIS (vegetation-impervious surface-soil) model for urban ecosystem analysis through remote sensing: comparative anatomy for cities. *International Journal of Remote Sensing*. **16** (12), 2165, **1995**.
23. GIBRIL M.B.A., BAKAR S.A., YAO K., IDREES M.O., PRADHAN B. Fusion of RADARSAT-2 and multispectral optical remote sensing data for LULC extraction in a tropical agricultural area. *Geocarto International*. **32** (7), 735, **2017**.
24. MISRA M., KUMAR D., SHEKHAR S. Assessing machine learning based supervised classifiers for built-up impervious surface area extraction from sentinel-2 images. *Urban Forestry & Urban Greening*. **53**, 126714, **2020**.
25. FU Y., LIU K., SHEN Z., DENG J., GAN M., LIU X., LU D., WANG K. Mapping impervious surfaces in town-rural transition belts using China's GF-2 imagery and object-based deep CNNs. *Remote Sensing*. **11** (3), 280, **2019**.
26. ABDI A.M. Land cover and land use classification performance of machine learning algorithms in a boreal landscape using Sentinel-2 data. *GIScience & Remote Sensing*. **57** (1), 1, **2020**.
27. CHEN C.-H., ZHAO W.-D., PANG T., LIN Y.-Z. Virtual metrology of semiconductor PVD process based on combination of tree-based ensemble model. *ISA Transactions*. **103**, 192, **2020**.
28. LIU C., ZHOU S., WANG Y.-G., HU Z. Natural mortality estimation using tree-based ensemble learning models. *ICES Journal of Marine Science*. **77** (4), 1414, **2020**.
29. ZIANE A., DABOU R., NECAIBIA A., SAHOUANE N., MOSTEFAOUI M., BOURAIOU A., KHELIFI S., ROUABHIA A., BLAL M. Tree-based ensemble methods for predicting the module temperature of a grid-tied photovoltaic system in the desert. *International Journal of Green Energy*. **18** (13), 1430, **2021**.
30. ALTHUWAYNEE O.F., PRADHAN B., PARK H.-J., LEE J.H. A novel ensemble decision tree-based Chi-squared Automatic Interaction Detection (CHAID) and multivariate logistic regression models in landslide susceptibility mapping. *Landslides*. **11**, 1063, **2014**.
31. FAN J., YUE W., WU L., ZHANG F., CAI H., WANG X., LU X., XIANG Y. Evaluation of SVM, ELM and four tree-based ensemble models for predicting daily reference evapotranspiration using limited meteorological data in different climates of China. *Agricultural and Forest Meteorology*. **263**, 225, **2018**.
32. ZHAI B., CHEN J. Development of a stacked ensemble model for forecasting and analyzing daily average PM_{2.5} concentrations in Beijing, China. *Science of the Total Environment*. **635**, 644, **2018**.
33. JIANG Y., WANG J., ZHANG L., ZHANG G., LI X., WU J. Geometric processing and accuracy verification

- of Zhuhai-1 hyperspectral satellites. *Remote Sensing*. **11** (9), 996, **2019**.
34. HUANG C., TAN L., LIU J., YAN K. Multi-Temporal-InSAR Ground Deformation Mapping of Beijing Subway Network Based on ALOS-2 and Sentinel-1 Data. *Polish Journal of Environmental Studies*. **2024**.
 35. FENG L., LI J., GONG W., ZHAO X., CHEN X., PANG X. Radiometric cross-calibration of Gaofen-1 WFV cameras using Landsat-8 OLI images: A solution for large view angle associated problems. *Remote Sensing of Environment*. **174**, 56, **2016**.
 36. PI Y., YANG B., LI X., WANG M., CHENG Y. Large-scale planar block adjustment of GaoFen1 WFV images covering most of mainland China. *IEEE Transactions on Geoscience and Remote Sensing*. **57** (3), 1368, **2018**.
 37. WANG B. Applying Machine-Learning Methods Based on Causality Analysis to Determine Air Quality in China. *Polish Journal of Environmental Studies*. **28** (5), 3877, **2019**.
 38. LIANG W., LUO S., ZHAO G., WU H. Predicting hard rock pillar stability using GBDT, XGBoost, and LightGBM algorithms. *Mathematics*. **8** (5), 765, **2020**.
 39. MANDAL S., KHAN D.A., RAUT R.D. 15 GBDT-Based Approach. *Cloud of Things: Foundations, Applications, and Challenges*. CRC Press. **2024**.
 40. HE J., SHI Y., XU L., LU Z., FENG M., TANG J., GUO X. Exploring the scale effect of urban thermal environment through XGBoost model. *Sustainable Cities and Society*. **114**, 105763, **2024**.
 41. CHOUDHURY A., MONDAL A., SARKAR S. Searches for the BSM scenarios at the LHC using decision tree-based machine learning algorithms: a comparative study and review of random forest, AdaBoost, XGBoost and LightGBM frameworks. *The European Physical Journal Special Topics*. **233** (2), **2024**.
 42. SUN H., WANG L., LIN R., ZHANG Z., ZHANG B. Mapping plastic greenhouses with two-temporal sentinel-2 images and 1d-cnn deep learning. *Remote Sensing*. **13** (14), 2820, **2021**.
 43. O'NEIL-DUNNE J.P., MACFADEN S.W., ROYAR A.R., PELLETIER K.C. An object-based system for LiDAR data fusion and feature extraction. *Geocarto International*. **28** (3), 227, **2013**.
 44. HU Q., WU W., XIA T., YU Q., YANG P., LI Z., SONG Q. Exploring the use of Google Earth imagery and object-based methods in land use/cover mapping. *Remote Sensing*. **5** (11), 6026, **2013**.
 45. HE T., WANG S. Multi-spectral remote sensing land-cover classification based on deep learning methods. *The Journal of Supercomputing*. **77** (3), 2829, **2021**.
 46. SHAO Z., CHENG T., FU H., LI D., HUANG X. Emerging issues in mapping urban impervious surfaces using high-resolution remote sensing images. *Remote Sensing*. **15**, 2562, **2023**.
 47. DING N., ZHANG Y., WANG Y., CHEN L., QIN K., YANG X. Effect of landscape pattern of urban surface evapotranspiration on land surface temperature. *Urban Climate*. **49**, 101540, **2023**.
 48. SHAO Z., AHMAD M.N., JAVED A. Comparison of random forest and xgboost classifiers using integrated optical and sar features for mapping urban impervious surface. *Remote Sensing*. **16**, 665, **2024**.
 49. DABOVE P., DAUD M., OLIVOTTO L. Revolutionizing urban mapping: deep learning and data fusion strategies for accurate building footprint segmentation. *Scientific Reports*. **14**, 13510, **2024**.
 50. REN H., HUANG X., YANG J., ZHOU G. Improving 30-meter global impervious surface area (GISA) mapping: New method and dataset. *ISPRS Journal of Photogrammetry and Remote Sensing*. **220**, 354, **2025**.
 51. MONDAL N., ANAND P., KHAN A., DEB C., CHEONG D., SEKHAR C., NIYOGI D., SANTAMOURIS M. Systematic review of the efficacy of data-driven urban building energy models during extreme heat in cities: Current trends and future outlook. In *Proceedings of the Building Simulation*, pp. 695-722, **2024**.
 52. GUPTA N., PANCHAL V. Artificial intelligence for mixed pixel resolution. *IEEE, Vancouver, BC, Canada*, **2011**.
 53. NICHOLS C.T. Land use/land cover classification: Methods to overcome pixel confusion and the effects of tree shadows in very high resolution multispectral imagery. *Maryville: Northwest Missouri State University*. **2012**.
 54. SUN D., GAO G., HUANG L., LIU Y., LIU D. Extraction of water bodies from high-resolution remote sensing imagery based on a deep semantic segmentation network. *Scientific Reports*. **14** (1), 14604, **2024**.
 55. CAO H., TIAN Y., LIU Y., WANG R. Water body extraction from high spatial resolution remote sensing images based on enhanced U-Net and multi-scale information fusion. *Scientific Reports*. **14** (1), 16132, **2024**.
 56. ZHANG D., YUE P., YAN Y., NIU Q., ZHAO J., MA H. Multi-Source Remote Sensing Images Semantic Segmentation Based on Differential Feature Attention Fusion. *Remote Sensing*. **16** (24), 4717, **2024**.
 57. AHMAD M.N., SHAO Z., XIAO X., FU P., JAVED A., ARA I. A novel ensemble learning approach to extract urban impervious surface based on machine learning algorithms using SAR and optical data. *International Journal of Applied Earth Observation and Geoinformation*. **132**, 104013, **2024**.